Pixelated On-Chip Amorphous Silicon Polarizers for Near Infrared Imaging on CMOS Image Sensors

Raphaël Mulin[1,3,4], Olivier Jeannin[2], Clémence Jamin-Mornet[3], Matthieu Boffety[4], and Jérôme Vaillant[3]
[1]*STMicroelectronics, 850 rue Jean Monnet, Crolles, F-38926, France*
[2]*STMicroelectronics, 12 rue Jules Horowitz, Grenoble, F-38000, France, email: olivier.jeannin@st.com*
[3]*Université Grenoble Alpes, CEA-Leti, F-38000 Grenoble, France*
[4]*Univ. Paris-Saclay, IOGS, CNRS, Laboratoire Charles Fabry, F-91127, Palaiseau, France*

***Abstract*—This paper presents the design, fabrication, and characterization of dielectric-based polarization-sensitive sensors, focusing on the integration of optical metasurface-based polarization routers compared to polarization filters for enhanced imaging performance. The proposed designs, fabricated on a backside-illuminated (BSI) CMOS image sensor, demonstrate high transmission and a polarization extinction ratio of 1.8 for an F/2 aperture at 940 nm. We investigate the advantages of polarization routers over traditional metallic or dielectric gratings filters highlighting their superior light collection efficiency. Experimental results show minimal spatial dispersion across the pixel matrix, confirming the robustness of the fabrication process. These results highlight the potential of on-chip dielectric polarization routers for advanced imaging applications, such as security, automotive, and medical imaging.**

***Index Terms*—CMOS Image Sensor (CIS), Polarization, Degree of linear polarization (DoLP), Angle of Polarization (AoP), polarization extinction ratio (PER), Quantum Efficiency (QE)**

I. Introduction

Polarization-sensitive imagers, often referred to as snapshot polarimeters, represent a cutting-edge category of cameras used in security, automotive, medicine or art [1]–[3]. Indeed, the polarization information can be used for various applications such as visual inspection (defect, stress), reflection removal, contrast enhancement or 3D reconstruction. Current commercial polarization-sensitive cameras use metallic polarization filters [4]. This wire-grid technology offers high polarization extinction ratio (PER) but at the cost of sensitivity. Parallel light against polarizer passes through, while perpendicular light is blocked (*i.e.* reflected or absorbed). In addition, for near-infrared (NIR) applications (typically around 940 nm), the quantum efficiency (QE) of those CMOS image sensors (CIS) decreases due the low absorption of silicon material. To address this limitation, we investigate fully dielectric polarization filters and polarization routers as an alternative to current metallic filters. As illustrated in Fig. 1, the proposed on-chip polarizers are based on process developed for metasurfaces in [5] and [6]. We use amorphous silicon (aSi) in silicon dioxide (SiO_2) since aSi material exhibits a high refractive index ($n = 3.8$) and very low extinction coefficient ($k < 10^{-3}$) at 940 nm. In addition, it is fully compatible with standard CMOS image sensor process, making it an ideal candidate for dielectric resonant structures.

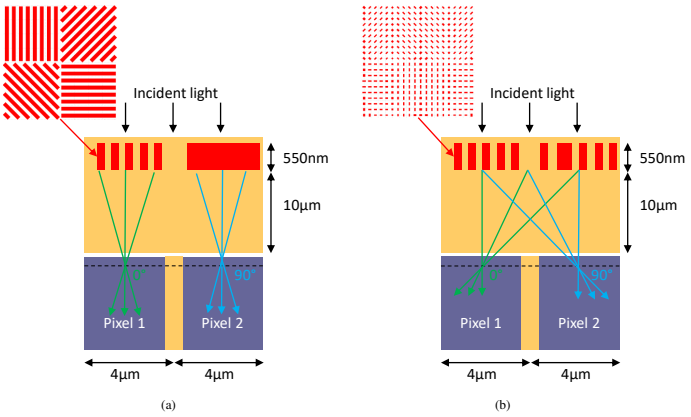

Fig. 1: $4\mu m$ Pixelated on-chip polarizers with (a) aSi in SiO_2 grid filters (b) aSi in SiO_2 optical metasurface routers

In this paper, we present the design and simulation of pixelated linear polarizers for $4\mu m$ backside-illuminated (BSI) pixels and their characterization.

II. Linear Polarizer Design

A. Linear polarization

The state of polarization (SoP) of light is characterized by the degree of polarization (DoP) and the angle of polarization (AoP). The Stokes vector is defined as $\boldsymbol{S}$=[S_0, S_1, S_2, S_3]$^\top$ and can be determined with a set of $n \geq 4$ intensity measurements $\boldsymbol{I}$=[I_0,...,I_n]$^\top$ that allow for the retrieval of SoP parameters. For this study, we will consider only linear polarization. The degree of linear polarization (DoLP) and the angle of polarization α can be expressed as

$$DoLP = \frac{\sqrt{{S_1}^2 + {S_2}^2}}{S_0}$$

$$\alpha = \frac{1}{2}\text{atan}\left(\frac{S_2}{S_1}\right) + \frac{\pi}{2}\text{sgn}(S_2)\frac{|\text{sgn}(S_1) - 1|}{2} \quad (1)$$

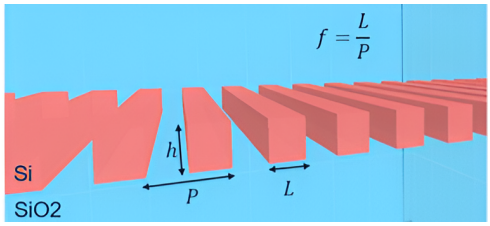

Fig. 2: Grating geometry parameters for polarization filtering: period P, width L, and height h (from [10])

with sgn, the signum function. The Stokes parameters are determined with four intensities obtained by measuring the linear polarization at the angles 0, $\pi/4$, $\pi/2$ and $3\pi/4$. For compactness and simultaneous acquisition, the image sampling is realized with a Bayer-scheme supercell design replacing the RGGB pattern with a 0°, 45°, 90°, 135° polarization pattern.

B. Design and simulation

On-chip pixelated dielectric polarization routers and filters were designed using methodologies based on electromagnetic simulations with the freeware RETICOLO, which implements the rigorous coupled wave analysis (RCWA) [7].

The operating principles of patterned dielectric polarization filters rely on coupling effect between Bloch modes within the structures providing high reflection. The design of such filters is straightforward. The first step is to simulate an infinite 1D silicon grating embedded in silicon dioxide and then to sweep the geometric parameters such as period P, width L, and height h (Fig. 2). We finally selected geometries that maximize their polarization selectivity.

Polarization routers have been designed with dielectric optical Metasurfaces (MS). Metasurfaces use the Huygens principle to deflect light through nanoelements called meta-atoms (with subwavelength size and period). When light passes through a meta-atom, the transmitted light acquires a phase delay which is locally controlled by the pillar diameter. Metasurfaces can be optimized to control light polarization using rotationally asymmetric meta-atoms: rectangular shaped meta-atoms will act differently for two orthogonal linear polarizations [8]. To design our polarization router, we used the traditional approaches relying on lookup tables (LUT) to shape spherical converging wavefront depending on polarization on top of each pixel.

As highlighted in [9], the operating principle of routers require to avoid energy coupling between modes, and it is thus recommended to limit the maximal width of pillars as well as the period separating them. In our previous work [10], we defined the ranges of period and width associated with these regimes for our materials (aSi/SiO_2) and our operating wavelength (940 nm).

Several designs for both polarization filters and routers have been generated and fabricated on a CMOS image sensor using process flow described in next section. Both operating principles rely on modal propagation of light through the structure to reflect or deflect light based on its polarization state. The aim of our work is to compare filters and routers performances after integration within pixels.

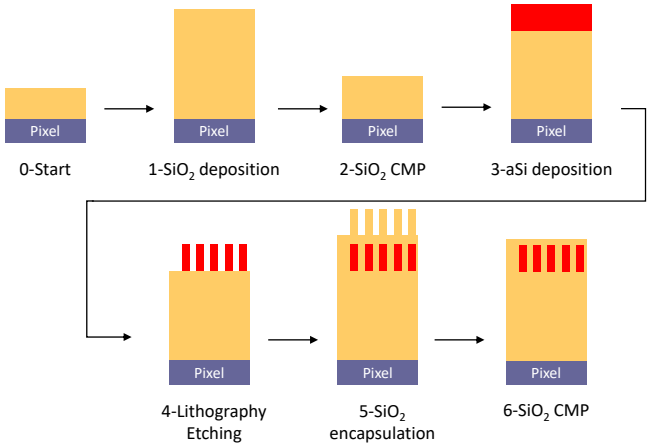

Fig. 3: On-chip pixelated polarization filter process flow

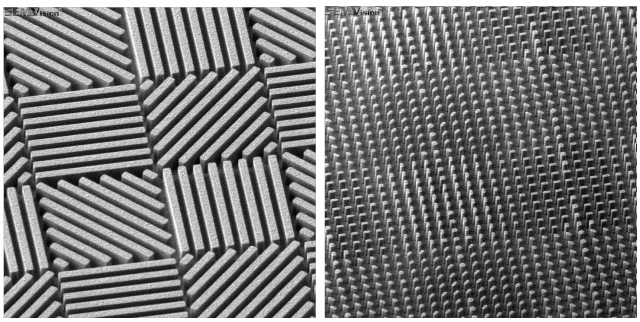

(a) (b)

Fig. 4: Tilted SEM view (Field of View: 4 pixels) of fabricated polarization (a) filters (b) router

C. Process on CMOS image sensor

In order to evaluate the performance of on-chip pixelated structures for both filter and router designs, we implemented them on a backside-illuminated image sensor. The polarizers are fabricated at wafer level, post-CMOS process, as an optical add-on. The process flow is described in Fig. 3.

Thus, we started by deposition and planarization of an optical pedestal: $10\mu m$ of low stress silicon oxide SiO_2, on which we place a layer of 550 nm of amorphous silicon aSi using PE-CVD. This layer is patterned using deep-UV immersion lithography and selective etching. With this process, we can target minimal dimension of 80 nm and minimal space of 90 nm. Then, the structures are encapsulated by silicon dioxide SiO_2 using PE-CVD followed by CMP planarization. The final step is the pad opening by etching the entire deposited stack above the pads.

A tilted SEM view of the fabricated on-chip pixelated polarization filters and routers is illustrated in Fig. 4 before SiO_2 encapsulation.

III. Characterization Results

The sensor testchip was characterized using a dedicated optical bench with a LED light source at $940\,\text{nm} \pm 10\,\text{nm}$

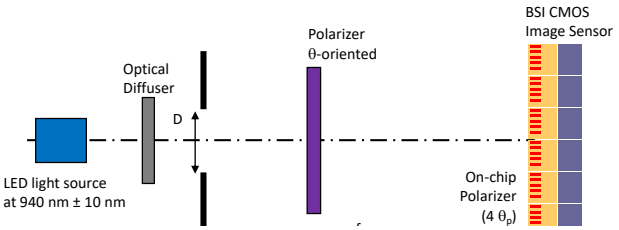

Fig. 5: Optical characterization bench schematics view. Sensor was illuminated with f/2 aperture ($D = 5\,\text{cm}$ and $f = 10\,\text{cm}$).

and an optical diffuser to uniformly illuminate the sensor with the on-chip polarizer (Fig. 5). The f-number of the illumination can be chosen by varying the distance f. The following characterization results are done with a challenging f/2 aperture illumination ($D = 5\,\text{cm}$ and $f = 10\,\text{cm}$).

The light is polarized with an external polarizer with a very high extinction ratio. This external polarizer is mounted on a rotation stage to control the angle of polarization θ_p of the input light during measurements.

The DoLP of the illumination setup is assumed to be equal to 1. We acquired images for polarizer orientations (θ) between 0 and 180° at intervals of 15°. For each orientation θ, we acquired $n = 1000$ images. The mean value $\bar{I}_{\theta,u,v}$ and the standard deviations σ_I of measurements were calculated as

$$\bar{I}_{\theta,u,v} = \frac{1}{n}\sum_{i=1}^{n} \hat{I}_{i,\theta,u,v}$$

$$\sigma_I{}^2 = \frac{1}{n-1}\sum_{i=1}^{n}\left(\hat{I}_{i,\theta,u,v} - \bar{I}_{\theta,u,v}\right)^2 \qquad (2)$$

where $\hat{I}_{i,\theta,u,v}$ is the collected number of electrons for a pixel of coordinates (u, v) in a region of interest (ROI) of 40 x 40 pixels for each of the 4 angles of polarization in the design, at the polarizer orientation $\theta \in$[0°,180°] in the image denoted $i \in$[1,1000].

Fig. 6 and Fig. 7 show the measurements obtained for the central super-pixel (*i.e.* group of four pixels with four orientations) of the ROI, corresponding to the filter and router designs, respectively. Error bars show the dispersion of values for the same type of pixel in the matrix (n = 1000 images). It should be noted that the low extinction ratio of the filter is due to the pedestal value of 10 μm, optimized for the router design. These results demonstrate the benefit of the polarization router compared to filter design, providing a much better light collection and thus more signal. Polarization router also demonstrates a high tolerance to aperture since the design perform polarization sorting at f/2.

We assume that the CMOS pixel is not sensitive to polarization; therefore, the only polarization-sensitive component is the metasurface or grating polarizer, which follows Malus's Law [11]. The pixel output signal is

$$I_t \propto T_u S_0 \left[1 + \left(\frac{\eta-1}{\eta+1}\right) DoLP\cos(2\theta_p - 2\theta)\right] \qquad (3)$$

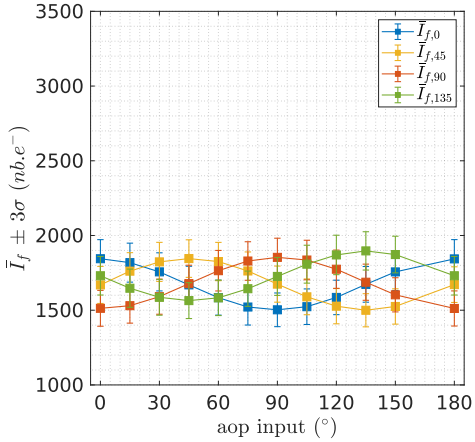

Fig. 6: Measured pixel response of the filter design versus illumination angle of polarization. Colors refers to 4 types of pixels, with metasurface sensitive to 4 different angles of polarization.

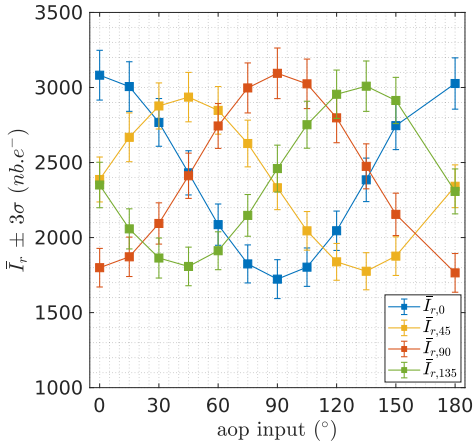

Fig. 7: Measured pixel response of the router design versus illumination angle of polarization. Colors refers to 4 types of pixels, with metasurface sensitive to 4 different angles of polarization.

S_0 refer to the first component of the Stokes vector of the incoming light, expressed in terms of the number of photons. θ_p is the orientation of the polarization pixel, θ is the angle of polarization of the external polarizer. η is the polarisation extinction ratio (PER) of the polarization pixels (*i.e.* the maximal divided by the minimal collected intensities depending on polarisation). T_u is the transmission of the filter or router to unpolarized light. From the perspective of collected signals,the only difference between a filter and a router is that (contrary to a router) transmission to unpolarized light of a filter depends on η.

For each pixel within the pixel matrix containing polarization routers, we used a gradient-based optimization to fit the polarization extinction ratio η and maximal transmission of pixels.

$$T_{\max} = T_u\left[1 + \left(\frac{\eta-1}{\eta+1}\right)\right] \qquad (4)$$

Fig. 8 shows the extinction ratio as function of the row

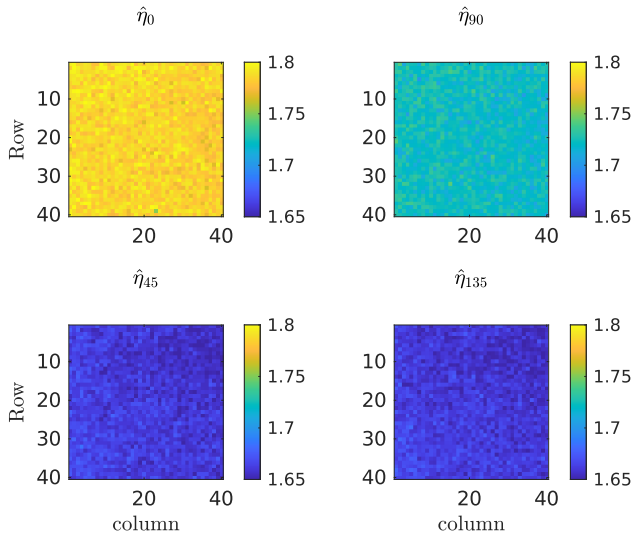

Fig. 8: Measured polarization extinction ratio (PER) non uniformity of router design for each pixel orientation (a) $\hat{\eta}_0$, (b) $\hat{\eta}_{90}$, (c) $\hat{\eta}_{45}$, (d) $\hat{\eta}_{135}$.

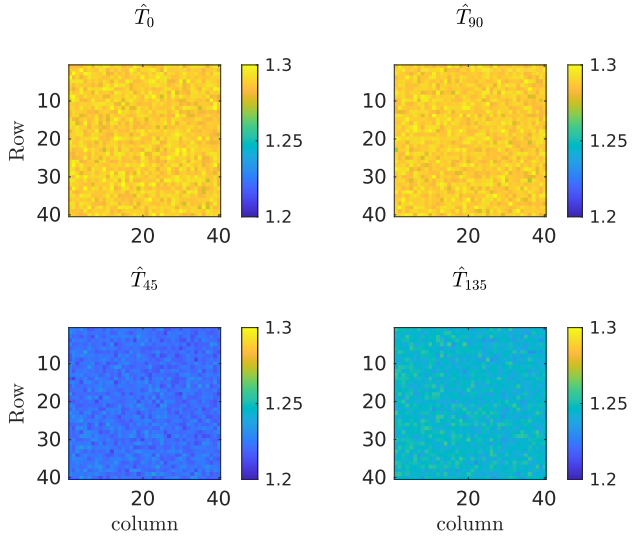

Fig. 9: Measured transmissions (for fully polarized light) normalized by sensitivity to unpolarized light of a reference zone without structures.

and column within the router design ROI on the sensor matrix. Due to the symmetries of the router, we expected that PER $\eta_0 = \eta_{90}$ and $\eta_{45} = \eta_{135}$. Measurements confirm this hypothesis considering 45° and 135° pixels but there is a difference of 0.05 between orientations of 0° and 90°. The extinction ratios slightly depend on pixel orientation, which could be explained by a partially polarized response of the pixel itself (due to asymmetrical Back-End). However, for a same pixel orientation, the spatial dispersion of our measurements is very low, demonstrating a low spatial dispersion of our process. Fig. 9 shows the relative transmission of polarizations routers as function of the row and column within the router design ROI on the sensor matrix. The transmission was normalized by a zone in the pixel matrix with no structuration, hence demonstrating up to 30% signal improvement.

IV. Conclusion and Perspectives

In conclusion, we have demonstrated the effectiveness of a dielectric-based polarization-sensitive sensor showing high transmission and a polarization extinction ratio of 1.8 for an f/2 aperture. The use of optical metasurface-based polarization routers shows significant improvements over traditional filters, improving light collection efficiency. The measurements confirm that the routers exhibit a high tolerance to aperture, with minimal spatial dispersion across the pixel matrix, thereby demonstrating the robustness of the fabrication process. These results highlight the potential of polarization routers for advanced imaging applications, particularly in security, automotive, and medical fields.

V. Acknowledgment

The authors gratefully acknowledge the contributions of the design and process integration team at STMicroelectronics and the platform at CEA-Leti for their contribution and support. The authors also gratefully acknowledge Laurent Coindoz and Cyril Bellegarde from the process integration team at CEA-Leti for their crucial contribution to the project and the SEM observations.

References

[1] A. D. Slepkov, "Painting in polarization," *American Journal of Physics*, vol. 90, no. 8, pp. 617–624, 08 2022. [Online]. Available: https://doi.org/10.1119/5.0087800

[2] C. Lei *et al.*, "Polarized reflection removal with perfect alignment in the wild," in *2020 IEEE/CVF Conference on Computer Vision and Pattern Recognition (CVPR)*, 2020, pp. 1747–1755.

[3] A. Dascalu and E. David, "Skin cancer detection by deep learning and sound analysis algorithms: A prospective clinical study of an elementary dermoscope," *EBioMedicine*, vol. 43, pp. 107–113, 2019. [Online]. Available: https://www.sciencedirect.com/science/article/pii/S2352396419302944

[4] T. Yamazaki *et al.*, "Four-directional pixel-wise polarization cmos image sensor using air-gap wire grid on 2.5-um back-illuminated pixels," in *2016 IEEE International Electron Devices Meeting (IEDM)*, 2016, pp. 8.7.1–8.7.4.

[5] L. Dilhan *et al.*, "Planar microlenses for near infrared cmos image sensors," *Electronic Imaging*, vol. 32, no. 7, pp. 144–1–144–1, 2020. [Online]. Available: https://library.imaging.org/ei/articles/32/7/art00004

[6] M. Lepers *et al.*, "Metasurface-based planar microlenses integrated on back-side illuminated cmos pixels," in *IISW proceedings*, 2023.

[7] J. P. Hugonin and P. Lalanne, "Reticolo software for grating analysis," 2021. [Online]. Available: https://arxiv.org/abs/2101.00901

[8] A. Arbabi *et al.*, "Dielectric metasurfaces for complete control of phase and polarization with subwavelength spatial resolution and high transmission," *Nature Nanotech*, vol. 10, no. 11, pp. 937–943, Nov. 2015, publisher: Nature Publishing Group. [Online]. Available: https://www.nature.com/articles/nnano.2015.186

[9] C. Gigli *et al.*, "Fundamental limitations of huygens' metasurfaces for optical beam shaping," *Laser & Photonics Reviews*, vol. 15, no. 8, p. 2000448, 2021. [Online]. Available: https://onlinelibrary.wiley.com/doi/abs/10.1002/lpor.202000448

[10] R. Mulin *et al.*, "Bloch mode analysis of subwavelength polarizing planar optics," in *High Contrast Metastructures XII*, C. J. Chang-Hasnain *et al.*, Eds., vol. 12432, International Society for Optics and Photonics. SPIE, 2023, p. 1243204. [Online]. Available: https://doi.org/10.1117/12.2646194

[11] S.-Y. Lu and R. A. Chipman, "Interpretation of mueller matrices based on polar decomposition," *J. Opt. Soc. Am. A*, vol. 13, no. 5, pp. 1106–1113, May 1996. [Online]. Available: https://opg.optica.org/josaa/abstract.cfm?URI=josaa-13-5-1106